

Research Article

Pore Structure Characteristics and Permeability Prediction Model in a Cretaceous Carbonate Reservoir, North Persian Gulf Basin

Hao Lu ¹, Hongming Tang ¹, Meng Wang ², Xin Li,³ Liehui Zhang,⁴ Qiang Wang,⁵ Yulong Zhao,⁴ Feng Zhao,¹ and Jijia Liao¹

¹College of Earth Science and Technology, Southwest Petroleum University, Chengdu Sichuan Province 610500, China

²College of Chemistry and Chemical Engineering, Chongqing University of Science and Technology, Chongqing 401331, China

³Chengdu North Petroleum Exploration and Development Technology Company Limited, Chengdu Sichuan Province 610500, China

⁴State Key Laboratory of Oil and Gas Reservoir Geology and Development Engineering, Southwest Petroleum University, Chengdu Sichuan Province 610500, China

⁵Geological Exploration and Development Research Institute of Chuanqing Drilling Engineering Co., Ltd., Chengdu Sichuan Province 610500, China

Correspondence should be addressed to Hongming Tang; swpithm@vip.163.com and Meng Wang; wangmeng_cqust@126.com

Received 9 September 2020; Revised 31 December 2020; Accepted 27 January 2021; Published 16 February 2021

Academic Editor: Abdelraheem Mahmoud Aly

Copyright © 2021 Hao Lu et al. This is an open access article distributed under the Creative Commons Attribution License, which permits unrestricted use, distribution, and reproduction in any medium, provided the original work is properly cited.

Due to the diversity of pore types, it is challenging to characterize the Middle East's Cretaceous carbonate reservoir or accurately predict its petrophysical properties. In this paper, pore structure in the reservoir is first classified using a comprehensive method. Then, based on the identified pore structure types, a new permeability model with high prediction precision is established. The reservoir is dominated by 6 pore types, such as intergrain pores and moldic pores, and 6 rock types. Grainstone, algal packstone, algal wackestone, and foraminifera wackestone are porous rock types, and echinoderm wackestone and mudstone are nonporous rock types. The types of pore structure in the study area can be divided into four types. Type I has midhigh porosity and medium-high permeability due to its large throat, while type II has a fine throat type with midhigh porosity and midpermeability. Due to their isolated pores, the permeability is low in types III and IV, and out of these two, type III has better storage capacity. Movable fluid saturation calculated by the spectral coefficient method and r_{apex} can characterize the boundary between the connected pores and unconnected pores very well in the research area. It is not accurate enough to simply classify the pore structure by permeability and porosity. The combination of porosity, permeability, r_{apex} , flow zone indicator, and the reservoir quality index can effectively distinguish and classify pore structure types in noncoring wells. The characteristics of each pore structure type are consistent with those of the fractal dimension, which thereby proves the effectiveness of the pore structure classification. New permeability prediction models are proposed for different pore structure types, and good prediction results have been obtained. This study is of great significance for enhancing oil recovery.

1. Introduction

Cretaceous carbonate formation in the Persian Gulf Basin is one of the most important oil and gas reservoir formations in the world [1–3]. However, due to the diversity of pore types, it is difficult to accurately characterize and predict the petrophysical properties, and water flooding is not effective [4–11]. A better understanding of the reservoir's micro-

heterogeneity and characteristics of the pore structures could be of great significance for the development of the oilfield.

Pore structure encompasses a reservoir rock's geometry and distribution of pores and throats. It is a critical controlling factor for the petrophysical properties and multiphase-flow characteristics in reservoir rock [12, 13]. Previous researchers have done abundant investigations into pore

structure, proposed different parameters to characterize and classify pore structure, and proposed different pore permeability prediction models for different pore structure types [14–16]. The fabric in carbonate rock is complex and can be easily transformed during diagenesis, which results in the transformation of pore structure [17]. Nabawy et al. reviewed the relationship model between different pore structure parameters and the petrophysical properties in rock [18]. Skalinski and Kenter summarized the research results of geology, petrophysics, and reservoir engineering and proposed several pore classification methods for carbonate rocks by combining sedimentary structures and rock's physical properties [19]. Nooruddin et al. obtained good permeability prediction results when considering the influence of tortuosity on the seepage patterns of different pore structures [20]. Although there are many studies, the pore structures of carbonate rock are a problem that needs continuous study.

Many research results have been published about pore structure of Cretaceous carbonate in the Middle East reservoirs [21–23]. Marzouk et al. identified the pore structure and the rock texture of a carbonate reservoir in the Middle East by using a diagram derived from thin section analysis and mercury injection capillary pressure (MICP) [24]. Using MICP data, Cantrell and Hagerty identified a large number of micropores in Saudi Arabia's Arabian formation [25]. Clerke et al. combined MICP data with the Thomeer function in order to propose a new method that could classify the complex pore system of a large carbonate reservoir in Saudi Arabia, and the method could comprehensively reflect geological, petrophysical, and flow characteristics [26]. The Cretaceous carbonate reservoir in the H oilfield served as a basis for Xin et al. to study pore structure, thus allowing them to improve the flow unit identification method for oilfield reservoirs as well as propose a new pore permeability relationship model [27].

Pore structures can be qualitatively described through the use of thin sections, scanning electron microscope analysis (SEM), high-pressure mercury injection (HPMI) tests, and nuclear magnetic resonance (NMR) tests. The parameters obtained from HPMI data, such as r_{\max} (maximum pore throat radius), r_{35} (the pore throat radius that corresponds to 35% mercury saturation, and it is considered to be the basis for identifying reservoir flow units), and r_{apex} (obtained from Pittman's method), can be used to quantify the pore structure of rock [28]. NMR tests are used to evaluate the pore structure of rock through the transverse relaxation time (T_2) spectrum and thus to obtain the movable fluid saturation (S_{wm}). S_{wm} is usually calculated by the T_2 cut-off value ($T_{2\text{cut-off}}$) [29]; however, continuous studies show that when there is a diffusion of fluid molecules between the large and small pores, the effectiveness of the method will be loosed [30–32]. The new methods that have been proposed to overcome these problems still need to be verified [33–36].

In this paper, petrological analysis, petrophysical tests, SEM analysis, and HPMI and NMR tests are combined in order to study the following: (1) the characteristics of a reservoir's pore structure, including pore types and pore throat radius distribution; (2) the applicability of some existing pore throat structure parameters from the study area and how to

quantitatively characterize and divide the reservoir's pore structure using these parameters; (3) new permeability prediction models for each pore structure type; and (4) the controlling factors of the pore structures. This paper has important theoretical and practical value for the provision of theoretical support in the development of reservoirs in both the mentioned research area and in other regions with similar geological characteristics.

2. Geological Setting

The H oilfield is located in the northern part of the Persian Gulf Basin. It is an area without strong tectonic activities during the Cretaceous period and has thick bedded bioclastic limestone [37–40]. Due to the Zagros orogeny, the area was compressed in the Miocene epoch to form the H anticline (Figures 1(a) and 1(b)) [41, 42]. The K formation is 50–70 m thick (Figure 1(c)) and uncomfortably overlies the Mishrif Formation [37]. It can be further divided into four members: Kh_1 – Kh_4 [38]. The Kh_2 member is extremely heterogeneous with a large amount of calcareous bioclasts and lime mud in the formation [43–45]. The bioclasts include foraminifera, algae, bivalves, echinoderms, and lamellibranchiata while the content of clay minerals and dolomite is below 3% [41].

3. Materials and Methods

3.1. Materials. In this study, 100 core samples (plug samples that are about 2.5 cm in diameter and 7 cm long) were taken from 4 wells made in the K formation of the H oilfield (uniform sampling according to depth) (Figures 1(a) and 1(c)). All the samples were tested for porosity and permeability, and thin sections were made for each sample. Next, 50 samples were selected for SEM analysis, 15 samples (2.5 cm in diameter and 3 cm in length) were selected for HPMI tests, and another 15 samples (2.5 cm in diameter and 3.5 cm in length) were selected for NMR testing.

3.2. Methods. The routine petrophysical testing instrument used was the CMS-300 from Southwest Petroleum University's State Key Laboratory, and it was used under a confining pressure of 3.5 MPa. All the samples were tested for porosity and permeability, and thin sections were made for each sample. Next, 50 samples were selected. The composition, pore structure, and diagenesis of the rock were observed using a LV100PO polarization optical microscope at the Oil and Gas Reservoir Geology and Exploitation, Southwest Petroleum University's State Key Laboratory. The microscopic features of the rock were observed using a Quanta 450 ESEM scanning electron microscope in order to identify the rock's minerals, pore structures, and diagenesis. Alongside the use of a scanning electron microscope and thin section, the pore types were identified according to Choquette's classification [14].

HPMI testing uses a Quanta Chrome Poremers-60 high-pressure mercury intrusion apparatus. The pore throat radius distribution and related parameters were obtained from the HPMI tests, including r_{\max} , r_{35} , average pore radius (r_a), drainage pressure, sorting coefficient, and r_{apex} . The pore-

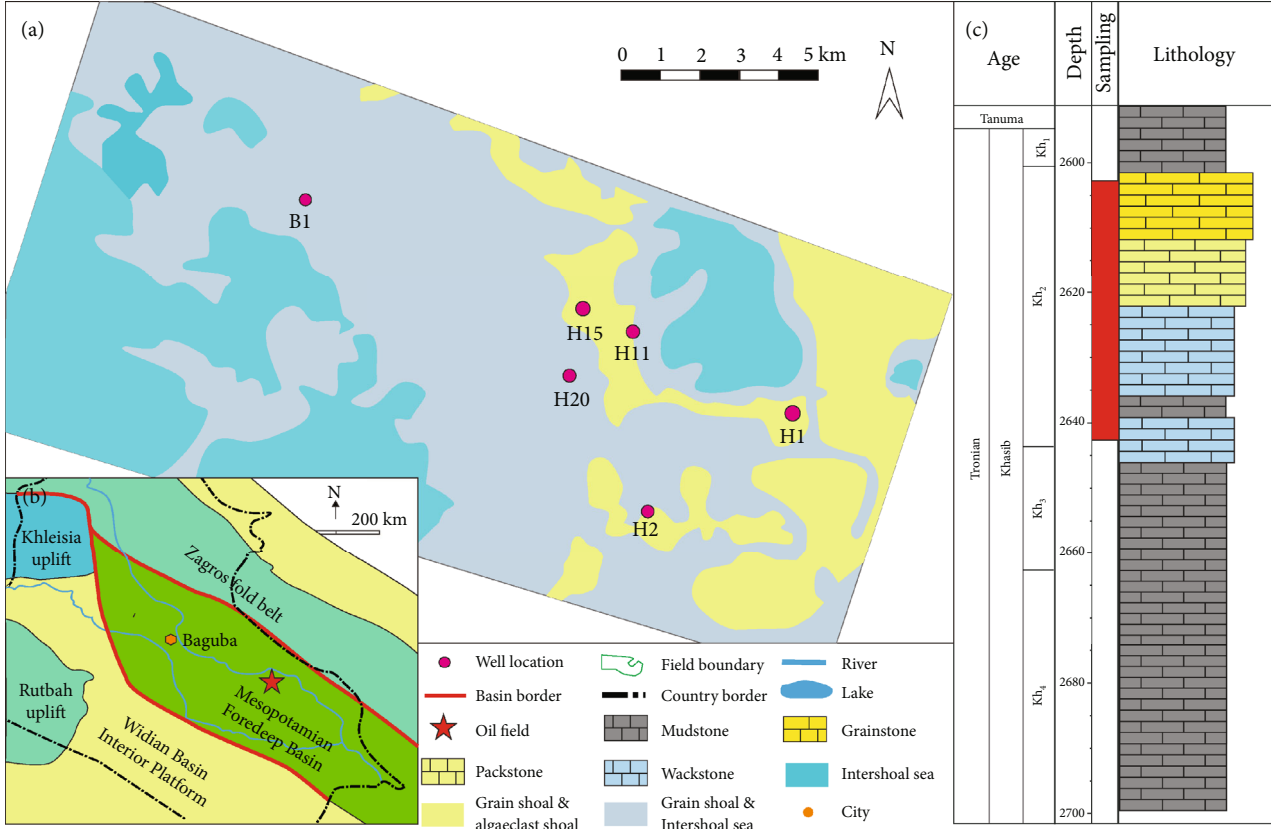


FIGURE 1: (a) Geographical location map of the H oilfield. (b) Regional tectonic map of the H oilfield. (c) Column chart of Kh₂ [36].

throat radius can be obtained using the Washburn equation as follows [23]:

$$R = \frac{2\sigma \cos \theta}{P_c}, \quad (1)$$

where R is the radius of the pore throat, σ is the interfacial tension, θ is the contact angle, and P_c is the capillary pressure.

Using the following equation, the permeability contribution for different pore-throat radii can be obtained from the HPMI data:

$$\Delta K_i = \frac{\Delta K_{mi}}{\sum_{i=1}^n \Delta K_{mi}}, \quad (2)$$

$$\Delta K_i = \frac{1}{2} \left(\frac{1}{p_{ci}^2} + \frac{1}{p_{ci+1}^2} \right) \Delta S_{i+1}, \quad (3)$$

where ΔK_i is the permeability contribution value of pore throat radii, i is the interval number of the pore throat radii, ΔS_{i+1} is the amount of mercury that intruded at different intervals, and p_{ci} is the capillary pressure at different intervals.

The NMR tests were performed using the nuclear magnetic analyzer MacroMR12-150H-I at Southwest Petroleum University's State Key Laboratory. After the samples were saturated with water, the tests were carried out at 25°C. The nuclear magnetic test's echo spacing was 0.09 ms, the number

of spin echoes was 12000, the number of signal superpositions was 128, the waiting time was 6 s, and the magnetic field strength was 0.3 T. The cores were then centrifuged using a GL-25MS with a centrifugal force of 400 psi in order to remove the mobile water and prepare for the second test. Both $T_{2cut-off}$ and the general coefficient method were used to estimate the movable fluid saturation. The saturation of movable fluid satisfies the following equation [46–50]:

$$BVI = \sum S_{wirr} (T_{2i}) \cdot P_i, \quad (4)$$

where BVI (%) represents the total immovable water saturation in the rock, $S_{wirr} (T_{2i})$ ($i = 1, 2, \dots, n$) represents the irreducible water saturation at each relaxation time point (%), and P_i is the signal amplitude that corresponds to T_{2i} (dimensionless).

$S_{wirr} (T_{2i})$ can be calculated by

$$\frac{1}{S_{wirr}} = mT_{2GM} + b, \quad (5)$$

where T_{2GM} is the geometric mean of the T_2 spectrum (ms) and m and b are coefficients.

By finding correlating statistical analyses, some scholars have obtained empirical formulas for sandstones and carbonates. Among them, the empirical formula applicable to carbonate rock is as follows:

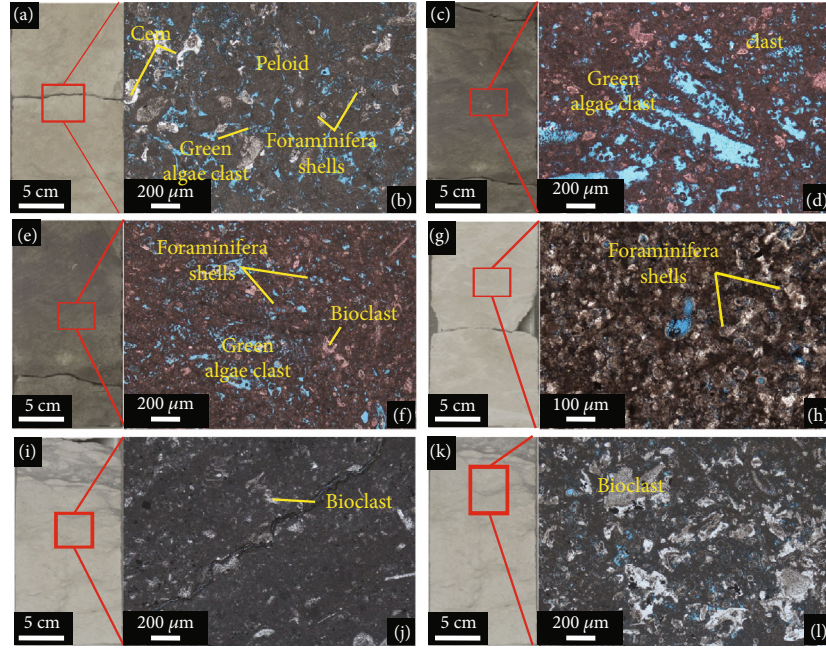


FIGURE 2: Rock type of the *K* formation: (a) and (b) are the core and the thin section picture of RT1 and H11 well (2604.00-2604.50 m), (c) and (d) are pictures of RT2 and H2 (2658.50-2658.65 m), (e) and (f) are pictures of RT3 and H11 (2614.35-2614.50 m), (g) and (h) are pictures of RT4 and B1 (2604.00-2604.15 m), (i) and (j) are pictures of RT5 (no visible pores) and B1 (2628.00-2628.50 m), and (k) and (l) are pictures of RT6 (no visible pores) and B1 (2628.00-2628.50 m).

$$\frac{1}{S_{\text{wirr}}} = 0.0113T_{2GM} + 1. \quad (6)$$

Amaefule et al. introduced the concept of the flow zone indicator (FZI) and reservoir quality index (RQI) [14]. The concept is based on pore throat, pore size, and grain size distributions, among other macroscopic parameters. If permeability is expressed in millidarcies and porosity is expressed as a fraction, the RQI can then be written as

$$\text{RQI} = \sqrt{\frac{K}{\phi_e}}, \quad (7)$$

where both FZI and RQI are in μm , K (md) is the permeability, and ϕ_e (%) is the effective porosity.

ϕ_z is the ratio of the pore volume to grain volume:

$$\phi_z = \frac{\phi_e}{1 - \phi_e}. \quad (8)$$

Thus, equation (7) can be written as

$$\text{RQI} = \phi_z \text{FZI}. \quad (9)$$

Taking the logarithm of equation (9) on both sides yields

$$\log \text{FZI} = \log \text{RQI} - \log \phi_z. \quad (10)$$

In addition, the fractal dimension has proven to be able to characterize the reservoir's pore structure characteristics

[30]; therefore, fractal dimensions were used to verify the effectiveness of pore structure classification.

4. Results

4.1. Rock Types and Pore Throat Types. Dunham's classification [51] is used to describe and classify rock types. Through a comprehensive study of cores, microscopic thin sections, and SEM photographs, it could be determined that the Khasib Formation in the study area consists of 6 major rock types: grainstone, algal packstone, algal wackestone, foraminifera wackestone, echinoderm wackestone, and mudstone. Among them, grainstone, algal packstone, algal wackestone, and foraminifera wackestone are porous rock types.

4.1.1. Grainstone (RT1). The main components of the rock are peloids, which account for more than 60%. They are mingled with bioclasts such as echinoderms, bivalves, and benthic foraminifera, which account for 20%-30%. Sparry calcite cementation developed in some pores. The diameter of the peloids ranges from 100 to 400 μm . The peloids are subrounded to rounded, with medium sorting. There is little mud filling in the pores (Figures 2(a) and 2(b)).

4.1.2. Algal Packstone (RT2). The proportion of bioclast content is greater than 50% of the total, and it is dominated by algal clasts. The diameter of algal clasts is between 50 and 300 μm . The species of algae are basically all green algae such as *Halimeda*. There are also some echinoderm and foraminifera clasts, accounting for about 15%. The lime mud filling between the clasts accounts for more than 30% (Figures 2(c) and 2(d)).

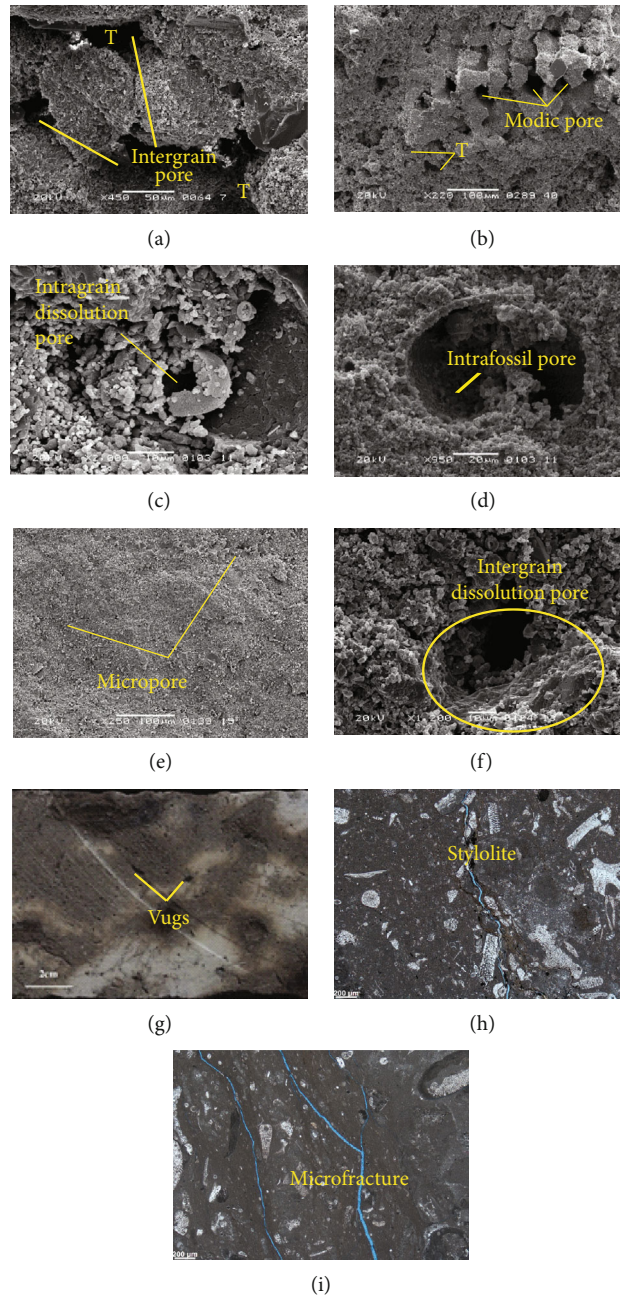


FIGURE 3: Reservoir pore systems of the *K* formation: (a) intergrain pore (RT1, H1, 2663.58 m); (b) moldic pore (RT2, H11, 2624.56 m); (c) intragrain dissolution pore (RT3, H2, 2621.25 m); (d) intrafossil pore (RT4, B1, 2642.51 m); (e) micropore (RT5, H2, 2605.42 m); (f) intergrain dissolution pore (RT1, H1, 2674.37 m); (g) vugs (RT2, H11, 2648.28 m–2648.41 m); (h) stylolite (RT6, H2, 2600.31 m); (i) microfracture (RT5, H2, 2599.55 m).

4.1.3. *Algal Wackestone (RT3)*. The clast type in RT3 is similar to that in RT2, but the content of clasts only accounts for about 30% in RT3. The content of mud crystal accounts for more than 70% (Figures 2(e) and 2(f)).

4.1.4. *Foraminifera Wackestone (RT4)*. The content of clasts in RT4 is between 10 and 50%, and it is dominated by foraminifera, which forms up to 50% of the total clasts in some samples. The species are mainly planktonic foraminifera, such as *Radiolaria* and *Globigerinae*. The clasts also include a small

amount of green algae and echinoderms, forming up about 10% of the total clasts (Figures 2(g) and 2(h)).

4.1.5. *Mudstone (RT5)*. The lime mud content exceeds 80%, even surpassing 95% on occasion. There are only a few bioclasts, including echinoderms, bivalves, and foraminifera. They are distributed and floating in the lime mud. The content of bioclasts here is less than 30% (Figures 2(i) and 2(j)).

4.1.6. *Echinoderm Wackestone (RT6)*. The clasts here are mainly echinoderm clasts, accounting for an average content

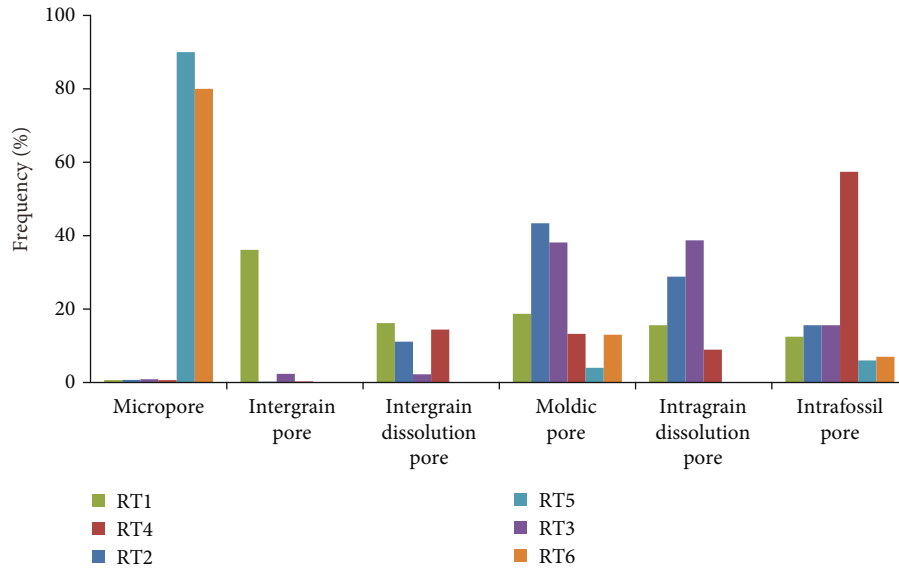


FIGURE 4: Frequency distribution of pore types in different rock types.

of 30%, while a small amount of algal clasts and foraminifera shell are also present, accounting for a content of about 10%. The core of RT6 is a dark-grey dense limestone with no visible pores on the surface (Figures 2(k) and 2(l)).

4.2. Pore and Throat Feature. Through the analysis of the thin section and SEM, it is clear that the main reservoir space in the study area is porous with very few vugs and fractures. The pore types are complex and diverse, and this is an important factor for reservoir heterogeneity. Lucia's classification [52] of carbonate reservoir pores is used to describe the pore types of the Kh₂ reservoir. A large number of moldic pores, intrafossil pores, and intergrain pores have developed in the reservoir, and there are also many types of throat.

(1) Intergrain pores

Intergrain pores have mainly developed in RT4 and RT5 and displayed good connectivity and a large pore diameter, which is generally between 0.01 mm and 0.3 mm (Figure 3(a)).

(2) Moldic pores

Moldic pores developed in the study area were mainly formed after selective dissolution of algal clasts. Most of them developed in RT2 and RT3, with some also developing, to varying degrees, in the remaining rock types. The pore size is generally between 0.02 mm and 0.2 mm (Figure 3(b)).

(3) Intragrain dissolution pores

This kind of pore is common in the studied reservoir, and the pore diameter is generally between 0.01 mm and 0.3 mm (Figure 3(c)). Most of these pores are half filled with calcite as the fluid inside the particles cannot be eliminated in time, indicating that they have low porosity.

(4) Intrafossil pores

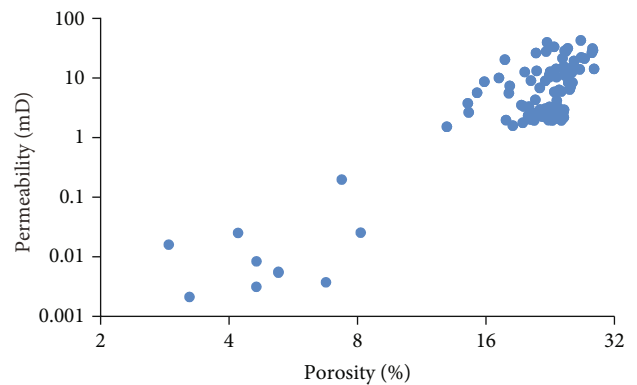


FIGURE 5: Crossplot of porosity versus permeability.

The intrafossil pores in the study area are mainly foraminifera intrafossil pores, which mostly developed in RT1, as well as developing to varying degrees in the remaining rock types. The pore size is generally between 0.02 and 0.1 mm (Figure 3(d)).

(5) Micropores

Micropores mainly exist between micritic calcites. The pore diameter is generally less than 1 μm , which has no contribution to the reservoir (Figure 3(e)).

(6) Intergrain dissolution pore

Intragrain dissolution pores can be seen near the erosion surface. They have a relatively large pore diameter, generally between 0.1 mm and 0.3 mm, and a very low filling degree (Figure 3(f)). The pore morphology is diverse.

(7) Vugs and fractures

TABLE 1: HPMI data of the *K* formation sample.

Well	Depth (m)	Φ (%)	<i>K</i> (mD)	SC	Special radius value (μm)					CMC _{apex} (%)
					r_{35}	r_{50}	r_{max}	r_a	r_{apex}	
H2	2647.90	21.81	101.00	2.84	17.65	12.45	26.75	12.28	16.32	90.00
H2	2648.23	12.35	83.40	3.91	16.00	3.60	26.75	9.10	13.98	87.03
H11	2609.12	12.31	57.72	3.00	6.60	4.62	21.38	6.85	16.00	85.54
H2	2646.63	18.19	30.90	4.24	2.50	0.97	10.69	2.82	6.30	93.88
H2	2647.27	18.35	16.70	2.22	1.50	0.89	5.33	1.36	4.00	95.71
H11	2609.78	21.47	11.79	2.59	1.74	1.09	5.33	1.44	2.50	93.26
H1	2664.45	24.48	20.00	3.86	4.00	0.10	5.33	1.52	4.00	98.28
H1	2668.04	24.97	10.90	2.46	1.00	0.59	3.75	0.91	2.50	95.32
H1	2662.62	24.53	12.10	1.99	1.00	0.58	3.83	0.97	2.53	94.03
H1	2659.64	22.31	8.93	2.61	1.00	0.68	3.83	1.06	2.49	95.13
H2	2644.81	22.36	1.48	1.47	0.39	0.30	1.57	0.38	1.00	93.63
H2	2674.29	20.60	0.43	1.59	0.25	0.20	0.43	0.19	0.25	94.16
H11	2611.41	26.66	8.11	1.89	0.40	0.51	3.78	0.75	2.50	96.2
H11	2611.96	22.74	5.56	2.59	1.00	0.43	3.77	0.82	2.50	97.53
B1	2669.36	23.13	2.02	1.12	0.16	0.23	1.09	0.25	0.63	95.38

Note: Φ : porosity; *K*: permeability; SC: sorting coefficient.

The study area is mainly a porous reservoir with few vugs. The vugs are usually distributed near the erosion surface, and their diameter is usually close to 2 mm (Figure 3(g)). Fractures include stylolite and microstructural fractures (Figures 3(h) and 3(i)), and both of them are developed in RT2 and RT3. The width of the fractures is generally 0.01 mm-0.05 mm.

Figure 4 shows that the 4 porous rock types and the 2 dense rock types have different pore type combinations. RT1 mainly has intergrain pores between peloids, as well as a few intrafossil pores, moldic pores, and intergrain dissolved pores (Figures 2(b) and 3(a)). The pore assemblage of RT2 and RT3 mainly consists of moldic pores and intragrain dissolved pores, with a small number of intrafossil pores and intergrain dissolved pores (Figures 2(d) and 2(f)). The pore assemblage of RT4 mainly consists of intrafossil pores and a small number of intragrain dissolved pores (Figure 2(h)). The pore assemblage of RT5 and RT6 mainly consists of micropores and a small number of intrafossil pores and intragrain dissolved pores (Figures 2(j) and 2(l)). Lucia et al. pointed out that the particle size of the rock has a direct impact on the pore structure, while different particle sizes and geometry will also have a direct effect on the physical properties of the rock [15]. Therefore, rock type is one of the factors indicating pore characteristics, and it can also provide the information on the environment that formed the pore structure.

4.3. Porosity and Permeability. The porosity and permeability in the study area vary greatly depending on rock types and show obvious zoning. RT1’s porosity is mainly concentrated in the range of 15.61-25.71%, with an average of 21.21%, and the permeability is mainly distributed between 10.00 and 100.00 mD, with an average of 67.52 mD. The permeability of RT2 and RT3 is concentrated between 2.50 and 50.49 mD with an average of 10.25 mD. RT4 displays obvious

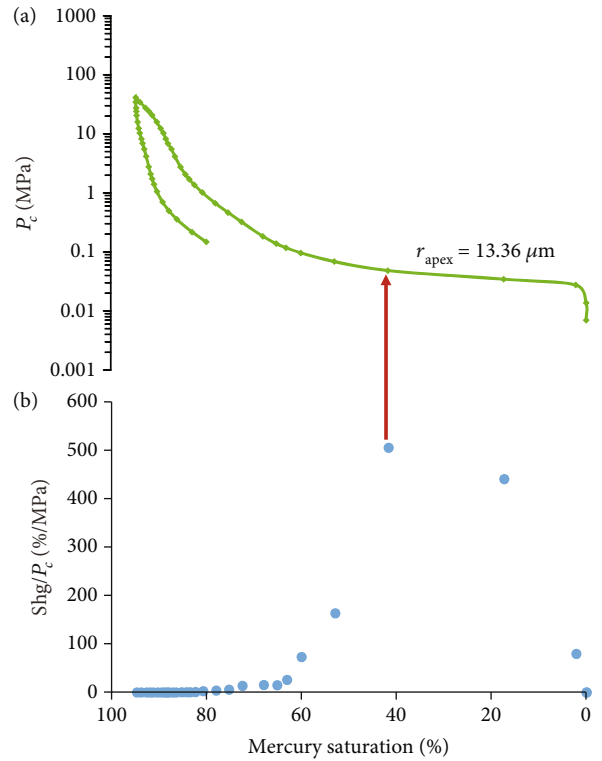


FIGURE 6: (a) Capillary pressure curve of the Khasib rock sample of the H oilfield (H11, 2609.12 m, RT1). (b) Pittman’s hyperbola shows an apex.

characteristics of high porosity and low permeability. RT4’s porosity is concentrated between 18.43 and 24.58%, with an average of 21.05%, while its permeability is mainly distributed between 1.73 and 3.22 mD, with an average value of

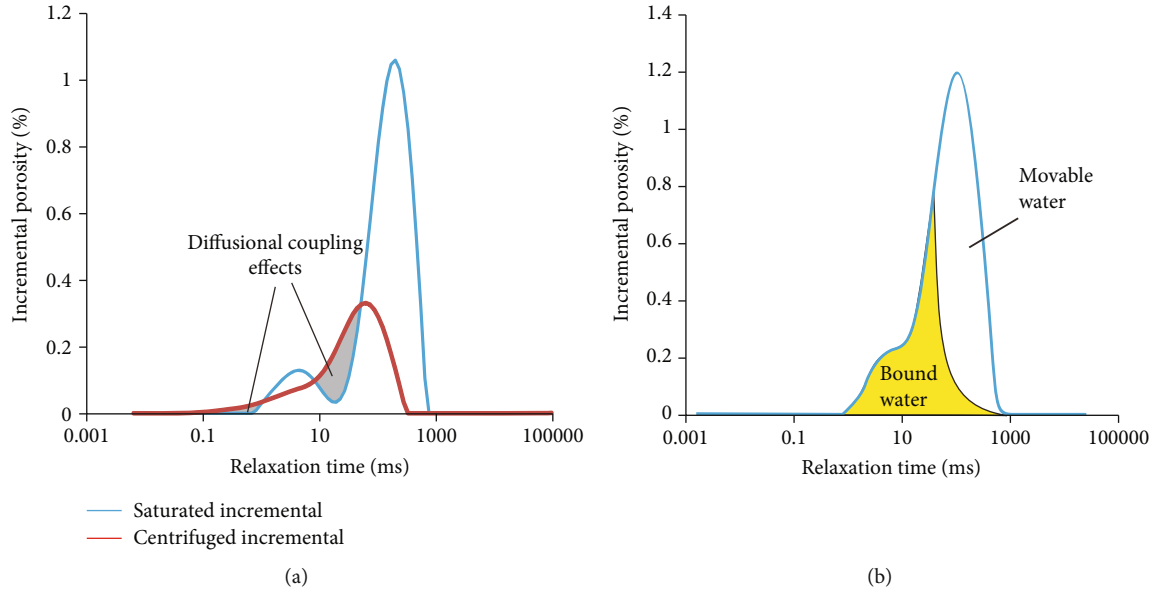


FIGURE 7: (a) Diffusion coupling effect (well H2, 2464.63 m, Kh_2). (b) Schematic diagram of irreducible water and movable water distribution [57].

TABLE 2: NMR data of the K formation sample.

Well	Depth (m)	Φ (%)	K (mD)	Movable fluid saturation (%)		Movable porosity	
				Spectrum coefficient method	T_2 cut-off value method	Spectrum coefficient method	T_2 cut-off value method
B1	2639.71	25.26	12.24	69.99	55.98	17.68	14.14
H1	2674.60	22.95	11.40	61.81	69.40	14.18	15.93
H2	2649.48	25.13	7.52	64.83	57.69	16.29	14.50
H1	2666.79	26.95	9.17	63.62	61.41	17.15	16.55
B1	2651.50	26.56	9.39	62.47	52.30	16.59	13.89
H1	2665.12	16.27	6.57	60.31	76.58	9.81	12.46
B1	2640.51	27.30	7.82	59.54	61.12	16.25	16.69
H1	2686.84	26.56	4.21	58.55	55.20	15.55	14.66
H1	2659.44	21.40	6.71	55.86	69.91	11.95	14.96
H2	2657.69	25.14	3.00	52.45	59.66	13.19	15.00
B1	2647.26	25.42	5.68	50.35	42.21	12.80	10.73
B1	2635.64	20.22	2.16	49.99	43.42	10.11	8.78

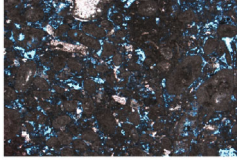
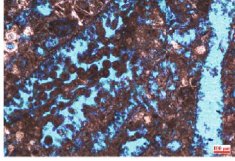
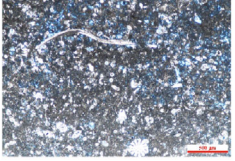
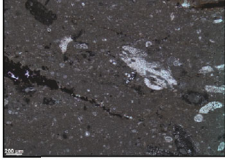
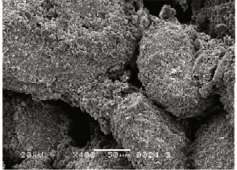
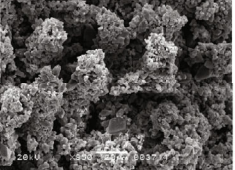
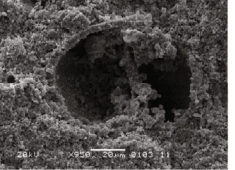
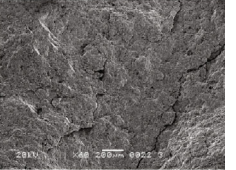
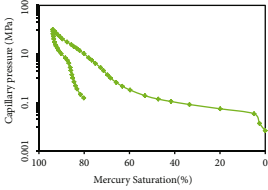
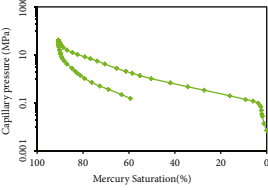
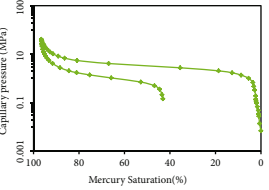
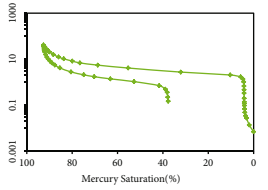
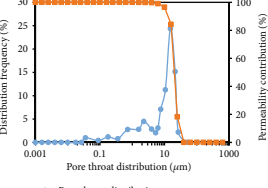
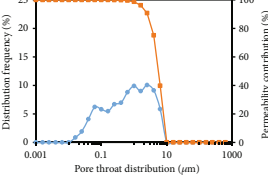
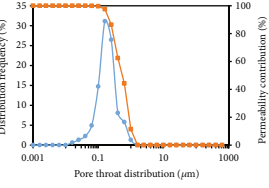
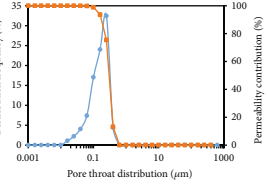
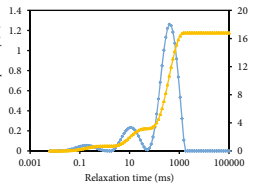
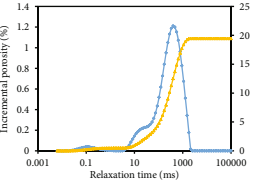
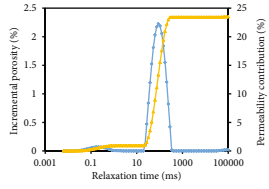
2.21 mD. RT5 and RT6's porosity is below 8.00%, and their permeability is below 0.30 mD (Figure 5).

4.4. *HPMI*. Previous works have defined many parameters in order to describe the throat structure of a pore [17, 53–56]. The experimental results show that RT1's r_{\max} is between 26.75 and 21.38 μm , with an average of 24.08 μm , while the average radius of a pore's throat (r_a) is 12.28–6.85 μm , with an average of 9.10 μm . The mercury injection curve shows that there are two platform sections in the mercury injection curve. RT2 and RT3's mercury injection characteristics are similar. Specifically, their r_{\max} is 3.75–10.69 μm , with an

average of 7.37 μm , their r_a is 0.91–2.82 μm , with an average of 1.94 μm , and the mercury injection curve has no obvious platform section. RT4's r_{\max} is 0.43–3.78 μm , with an average of 2.04 μm , and its r_a is 0.19–0.82 μm , with an average of 0.53 μm . RT4's mercury injection curve shows that the platform section in the middle of the HPMI curve has a wide range, and the sorting coefficient is close to 1 (Table 1).

Pittman's hyperbola shows an apex, and the throat radius corresponding to this point is r_{apex} (Figures 6(a) and 6(b)). The HPMI data show that RT1's r_{apex} is distributed in a range greater than 13.00 μm , and the CPC_{apex} (cumulative permeability contribution rate of pores with a throat radius greater

TABLE 3: Characteristics of each pore structure type.

	Type I	Type II	Type III	Type III
Pore throat structure classification	Mid-high porosity, mid-high permeability, large throat	Mid-high porosity mid permeability mid throat	Mid-high porosity low permeability fine throat type	Ultra low porosity and ultra low permeability fine throat type
Rack type	RT1	RT2,RT3	RT4	RT5,RT6
Pore type	Mainly intergrain pores with few moldic pore and intrafossil pore	Mainly moldic pore and intragrain dissolved pore with few intrafossil pore	Intrafossil pore with few moldic pore	Micro pore
Casting thin sections picture				
SEM picture				
Mercury injection curve				
Pore throat radius and permeability distribution				
Nuclear magnetic T2 spectrum				No sample

than r_{apex}) is between 85.54 and 90.00%. RT2's r_{apex} is distributed from 4.00 μm to 6.30 μm , and the CPC_{apex} changes from 85.54% to 90.00%. RT3's r_{apex} is about 2.50 μm , and the CPC_{apex} is between 94.03 and 95.32%. RT4's r_{apex} is mainly distributed in a range smaller than 2.50 μm , and the CPC_{apex} is greater than 95%.

4.5. NMR. All the data from the 15 samples showed the diffusion coupling phenomenon (Figure 7(a)), and so the spectral coefficient method was proposed in order to calculate the amount of bound water and movable water. Figure 7(b) shows the distribution of bound water in the rocks [57].

The T_2 spectrum of RT1 has a right-skewed bimodal pattern, and the higher peak's relaxation time of the T_2 spectrum is greater than 100 ms. The movable water saturation is 61.81-69.99% with an average of 64.54%. The T_2 spectral characteristics of RT2 and RT3 are similar as they both show a right-skewed multipeak type with a large range of relaxation time, usually between 30 and 1000 ms. On the left of the T_2 spectrum, there is a smaller bulge with no distinct boundary between the peaks. RT2's movable water saturation is 55.86-64.83% with an average of 59.16%. RT4's T_2 spectrum is unimodal with relaxation time between 20 and 300 ms and movable water saturation between 49.99-52.45%, with an average of 53.21%, its pores are mainly comprised of small pores, and the sorting is better than others (Table 2).

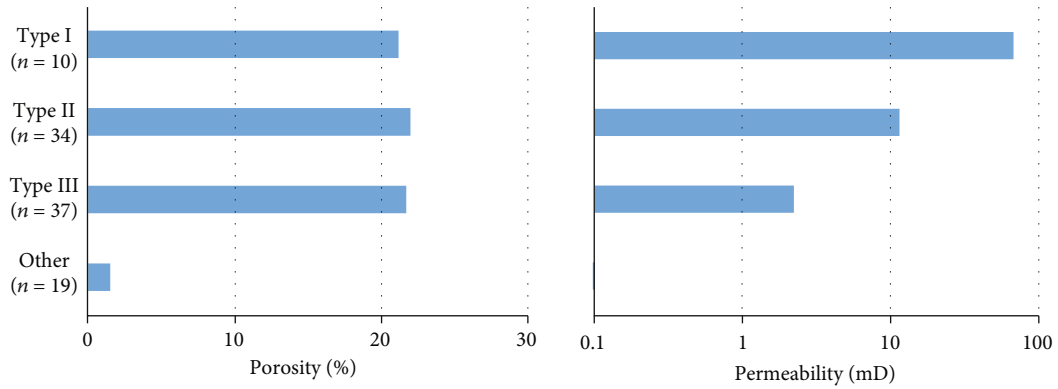


FIGURE 8: Average petrophysical property distribution of three pore throat structure types.

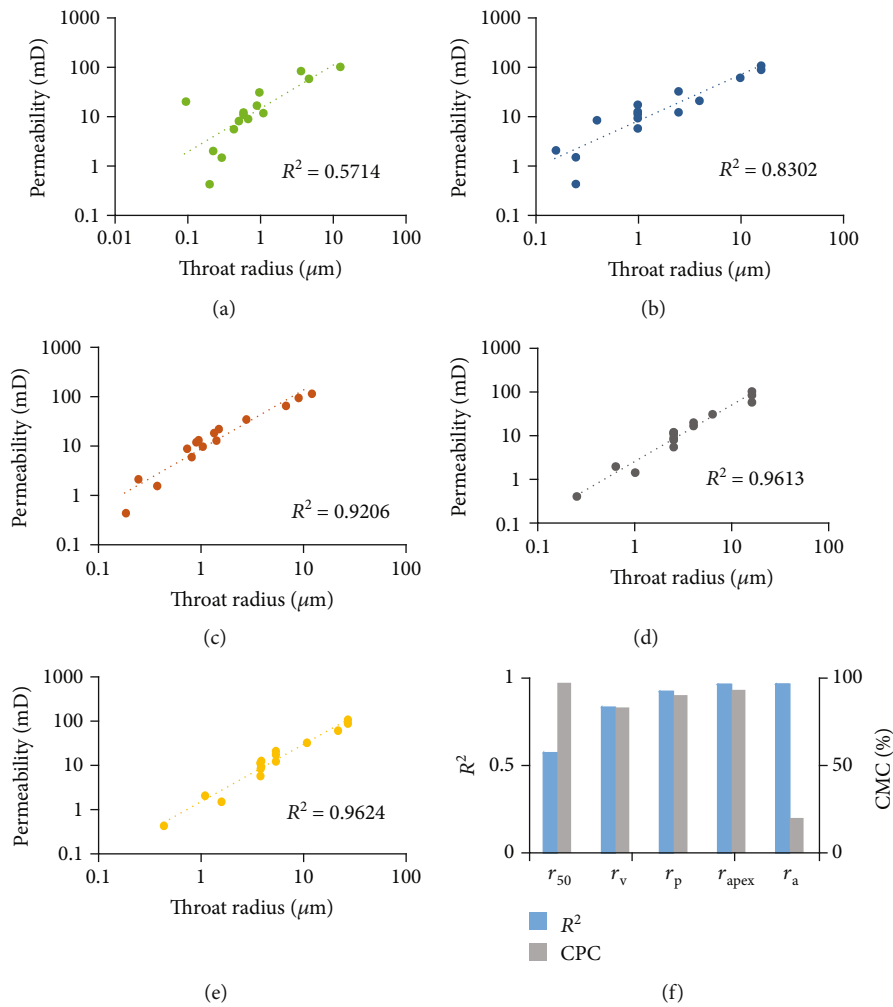


FIGURE 9: (a) Correlation between r_{50} and permeability. (b) Correlation between r_{35} and permeability. (c) Correlation between r_a and permeability. (d) Correlation between r_{apex} and permeability. (e) Correlation between r_{max} and permeability. (f) Comparison of correlation coefficient and cumulative permeability contribution rate.

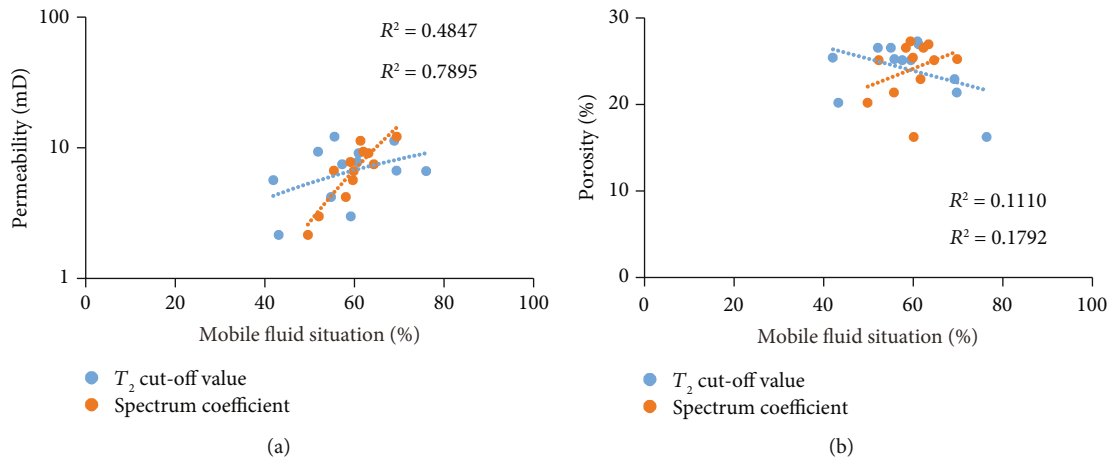


FIGURE 10: (a) Correlation of NMR movable fluid saturation and permeability calculated by two methods. (b) Correlation analysis of NMR movable fluid saturation and porosity calculated by two methods.

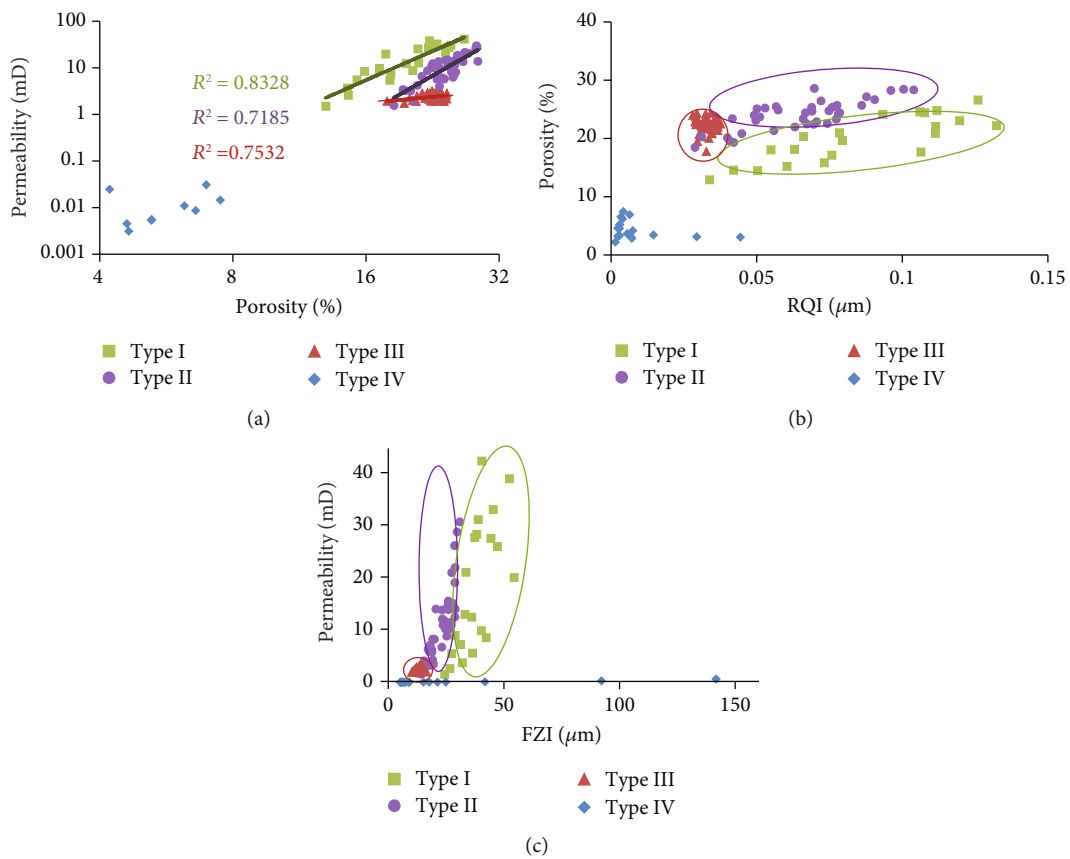
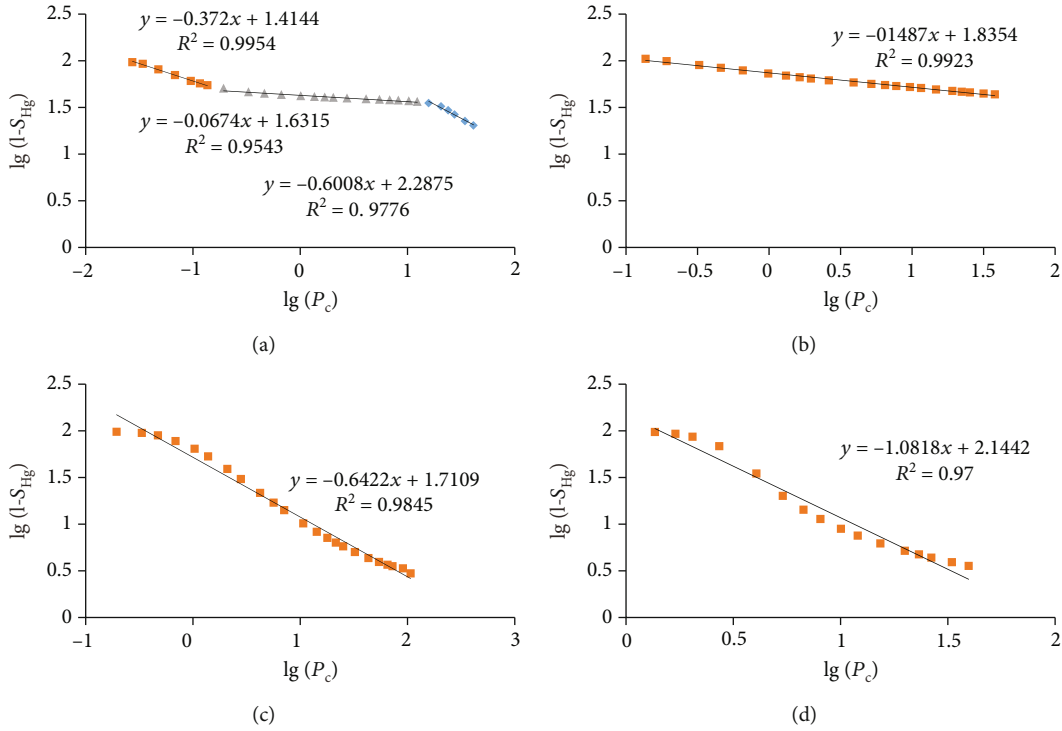


FIGURE 11: (a) Plot shows that porosity and permeability distribution of different pore structure types has obvious zoning. (b) Plot shows that RQI and porosity distribution of different pore structures has obvious zoning. (c) Plot shows that FZI and permeability distribution of different pore structures has obvious zoning.

TABLE 4: Quantitative classification of 4 pore structure types.

Pore structure type	Φ (%)	K (mD)	FZI (μm)	RQI (μm)	r_{apex} (μm)	S_{wm} (%)
Type I	10.00-22.89	>2.97	>19.85	>0.04	>2.83	>53
Type II	>22.89	>2.97	14.12-19.85	>0.04	>2.83	>53
Type III	17.84-24.04	2.02-2.97	<14.12	<0.04	0.3-2.83	<53
Type IV	<10.00	<0.5	—	—	<0.3	—

FIGURE 12: Representative sample plots of $\lg S_{\text{Hg}} - \lg P_c$ based on MICP data: (a) type I (well H2, 2464.63 m, Kh₂); (b) type II (well H1, 2664.45 m, Kh₂); (c) type III (well H11, 2611.41 m, Kh₂); (d) type IV (well B1, 2669.36, Kh₂).

5. Discussion

5.1. Classification of Pore Throat Structure

5.1.1. *Qualitative Classification of Pore Structure.* Through a comprehensive analysis, four pore structure types have been identified (Table 3).

Among the four pore structure types, types I, II, and III can all provide a reservoir space for oil and gas, while type IV hardly provides a reservoir space nor flow channel. Type I is the pore structure type with the best petrophysical properties. However, in the study area, the reservoir with type I is not very thick, with an average thickness of 1.5 m. This means that the reservoir cannot be highly productive, and on the contrary, it can easily lead to a poor water flooding effect on the adjacent layers that have poor petrophysical properties.

The porosity of types I, II, and III is similar, but their permeability decreases in turn. It thus can be inferred that the pore structure determines the seepage capacity of the rocks (Figure 8). Combined with the rock's thin section and SEM

analysis, there is a large amount of mud in types II and III, and it leads to a substantial fine throat. The pore heterogeneity in type II is strong, and it is likely that there will be a dominant channel, which will lead to a significant increase in residual oil saturation.

5.1.2. *Quantitative Classification of Pore Structure.* The radius of the throat between the pores is the determining factor for permeability [58–60]. The parameters listed in Table 1, such as r_{35} and r_{apex} , have been proven to correlate well with the reservoir properties in the previous study on clastic rock reservoirs [4, 14] and have also been applied to various oil and gas development methods such as the division of flow units and the classification of reservoir types [15, 16, 18].

Figures 9(a)–9(e) show the correlation analysis of the special radius value with permeability. The results show that r_a , r_{max} , and r_{apex} all correlate well with permeability, and the R^2 is all more than 0.9. r_{50} had the worst correlation with permeability while the average cumulative permeability contribution rate corresponding to r_{apex} is the highest, reaching

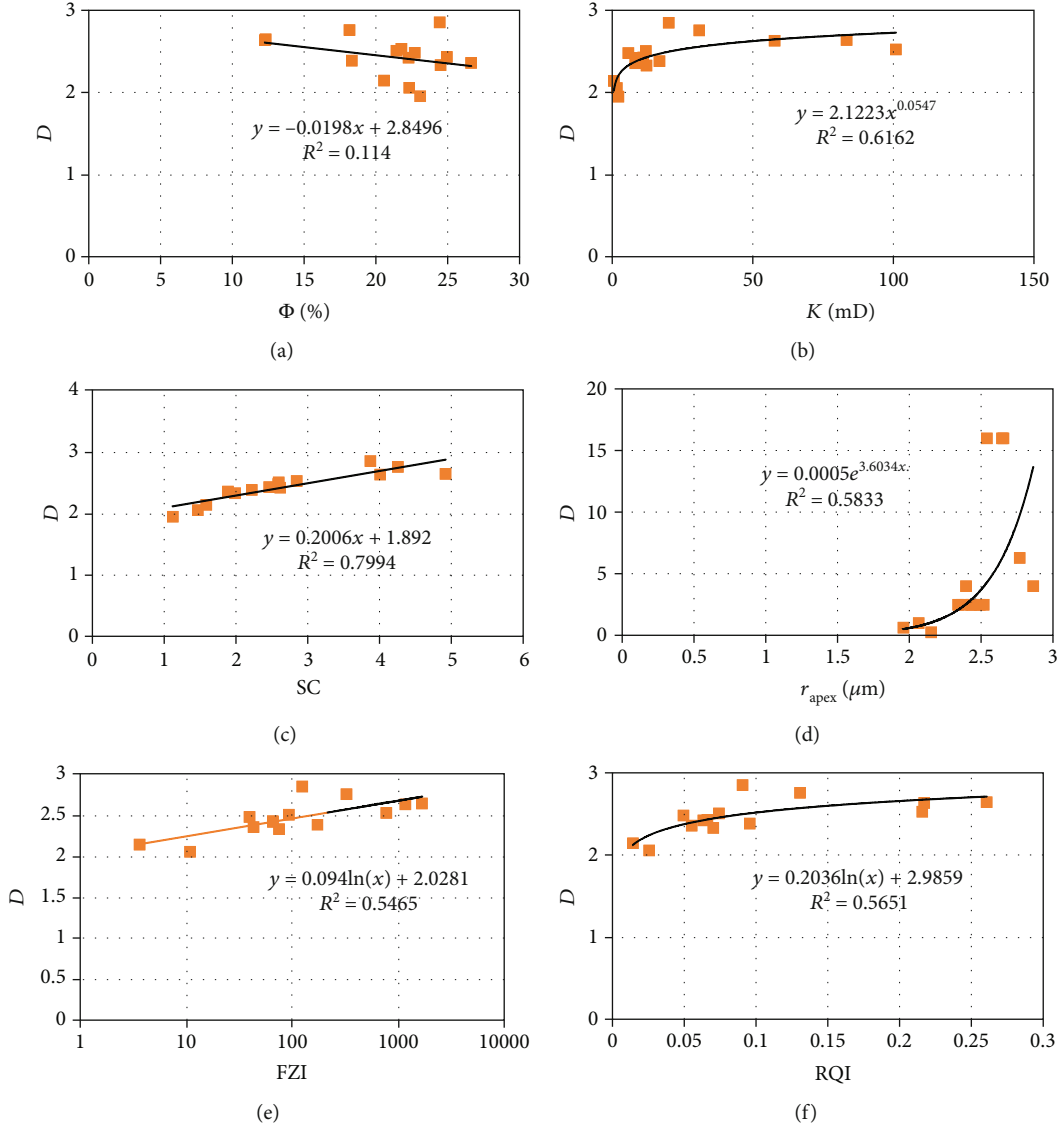


FIGURE 13: The relationships between the D of different petrophysical properties: (a) D versus air porosity; (b) D versus air permeability; (c) D versus SC; (d) D versus r_{apex} ; (e) D versus FZI; (f) D versus RQI.

93%, as shown in Figure 9(f). So it can be said that r_{apex} is the boundary value between the connected pores and unconnected pores. The mercury saturation corresponding to r_{apex} is less than 35%, which means that the permeability is only determined by a small number of large pore throats (the radius of pore throats is larger than r_{apex}).

The calculations made by the $T_{2cut-off}$ value of the bulk volume of irreducible fluid and the free fluid index are based on the isolated pore model [61, 62]. In rocks, both large pores and small pores are connected with each other, and the only difference is how good the connectivity is. Diffusion coupling is a phenomenon in which fluid molecules are diffused between large and small pores, and it results in the uniformization of the T_2 spectrum [63–66]. Some scholars believe however that the diffusion coupling effect invalidates the method used to calculate the movable water saturation through the $T_{2cut-off}$ value [23, 25]. In this study, NMR mov-

TABLE 5: Permeability prediction models of 4 pore structures types.

Pore structure type	Petrophysical model	Coefficient R^2
I	$K = 0.003e^{0.250\Phi}$	0.8
II	$K = 0.771e^{0.159\Phi}$	0.81
III	$K = 5.007e^{0.159\Phi}$	0.73
IV	$K < 0.5$	—

able fluid saturation is calculated using two methods and the results obtained are quite different (Table 2). As indicated in Figure 10(a), the correlation between permeability and movable fluid saturation (S_{wm}) that was calculated using the spectral coefficient method is the better of the two, with R^2 reaching 0.78, while the other's R^2 is only 0.48. This indicates that the spectral coefficient method that was proposed to

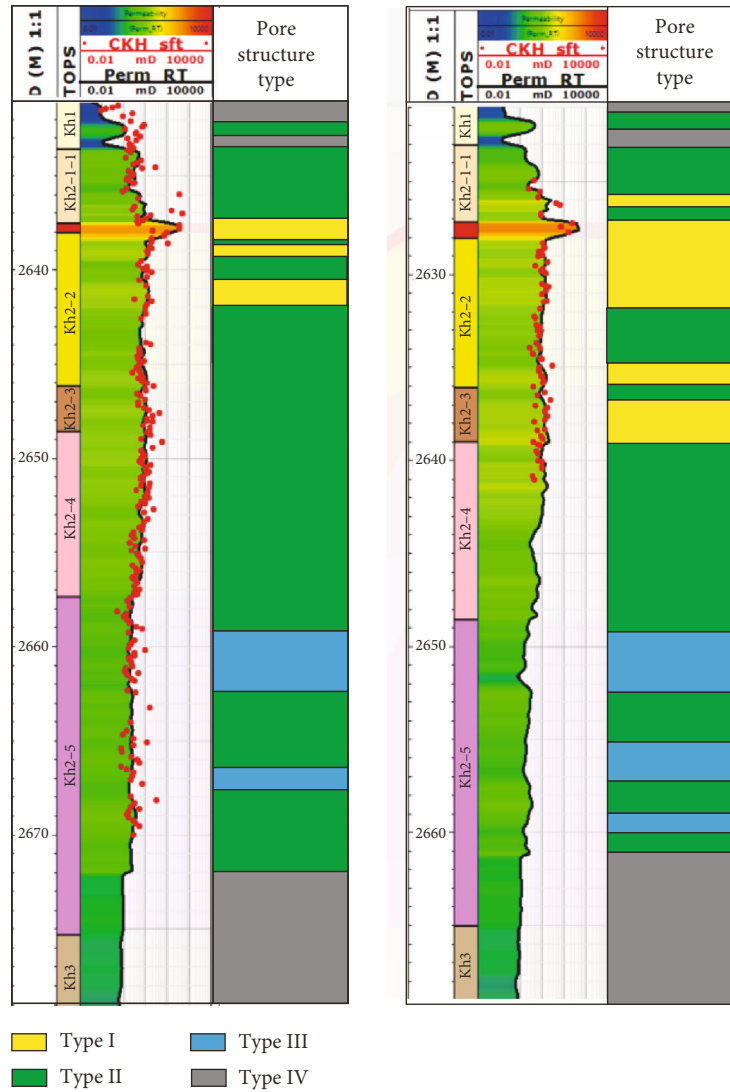


FIGURE 14: The results of permeability prediction for two wells.

eliminate the diffusion coupling effect is more suitable for carbonate reservoirs with diverse pore types. The correlation analysis of porosity and S_{wm} shows that porosity is basically independent of S_{wm} (Figure 10(b)).

Figure 11(a) shows the distribution of the porosity and permeability in different pore structures that have a good relationship between porosity and permeability. This information can improve the permeability prediction model's accuracy.

Although the porosity and permeability of different pore structures are well zoned and the correlation between porosity and permeability is good (Figure 11(a)), it was found that quantitatively dividing the pore structure by porosity and permeability alone is not accurate. This is because the porosity and permeability distribution range of different pore structure types is similar. Other methods, such as the flow zone indicator (FZI) and reservoir quality index (RQI), have been widely used in studies on reservoirs in recent years. For example, Rafiei et al.'s research shows that hydraulic flow unit classification based on FZI and RQI significantly

improved the normalization of capillary pressure curves [67]. Furthermore, Zhang et al.'s research on shale shows that FZI and RQI can be used to establish porosity-permeability transformations with high correlations [68]. FZI and RQI are usually used to identify flow units, and some studies on reservoirs in the Middle East show that these two parameters can significantly improve the normalization of capillary pressure curves and accurately indicate the difference of flow units [27, 67]. FZI and RQI denote the flow characteristics and reservoir characteristics of the reservoir, and the two parameters are also obviously suitable for the analysis of pore structure. Figures 11(b) and 11(c) show that the combination of RQI with porosity, as well as the combination of FZI with permeability, can differentiate the four pore structures well. Therefore, we can use this multiparameter combination method in order to quantitatively characterize the reservoir's pore structure in the study area, as well as propose a more accurate permeability prediction model for different pore structure types (Table 4).

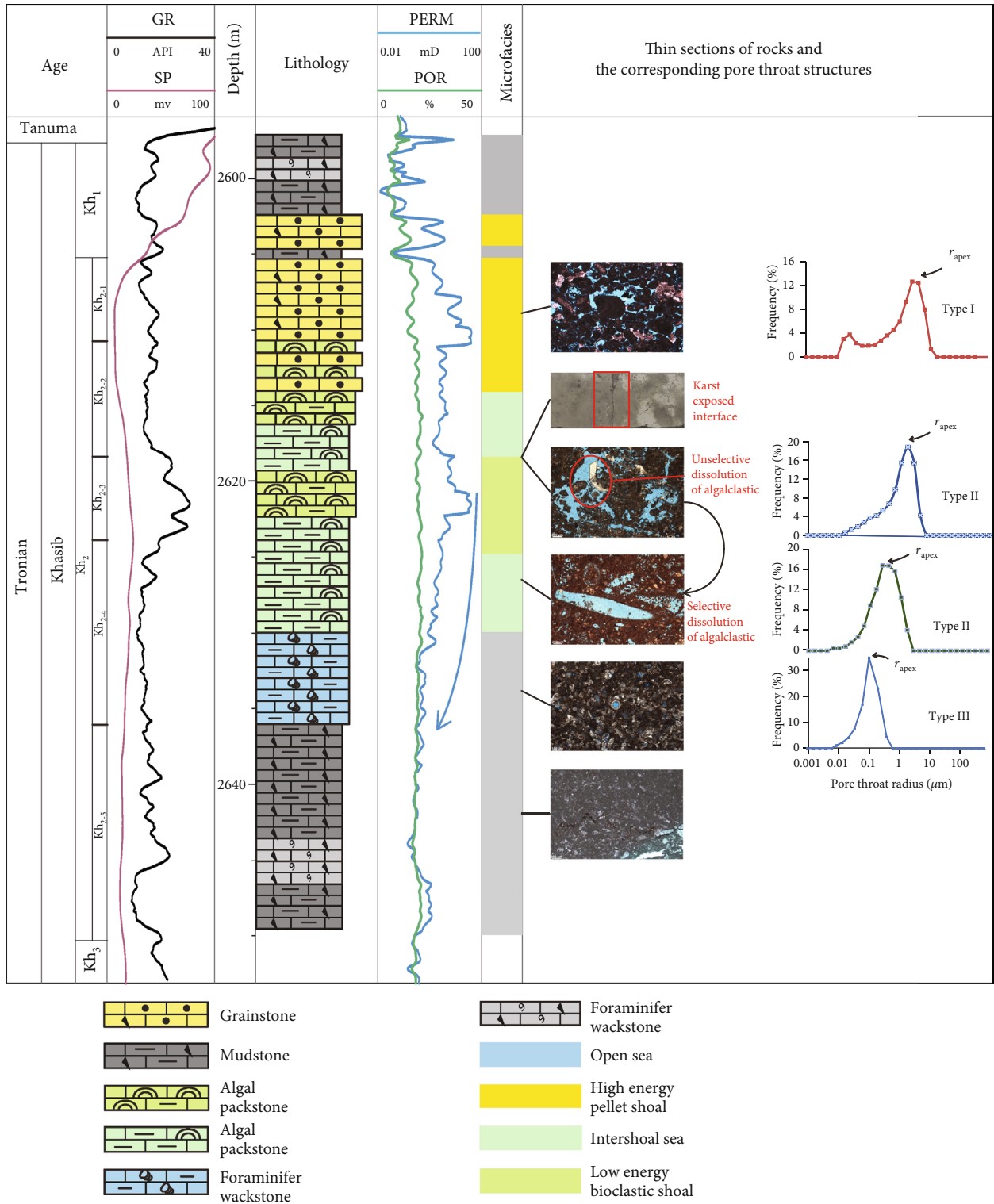


FIGURE 15: Comprehensive diagram of lithology and pore structure.

5.1.3. Classification Validity Analysis and Structural Feature Analysis. The fractal dimension (D) deduced from fractal theory can quantitatively evaluate pore surface roughness and structural irregularity [30, 69–72]. Many researchers have shown that D can be used to evaluate pore structure and analyze the influence factors of various reservoirs [69, 70]. The D of pores in a rock are always between 2 and 3, and the higher the D value, the more complex the pore structure.

In this study, we adopt the method reported by Li to compute D based on MICP data [71].

$$\lg(1 - S_{\text{Hg}}) = (D - 3) \lg P_c - (D - 3) \lg P_{\text{min}}, \quad (11)$$

where S_{Hg} is the accumulative mercury saturation (%), P_c is the capillary pressure (MPa), and P_{min} is the displacement pressure (MPa).

In this paper, the D of different pore structure types is obviously different. Figure 12(a) shows that the pore throat structure of type I has multifractal characteristics with three different slopes. This correlates with the many studies that have pointed out that pore structure has multifractal characteristics and thus indicates that there are great differences among macropores, mesopores, and micropores [30, 69]. In this paper, type I has been shown to have a variety of pore types, including macropores (intergrain pores, etc.), mesopores (dissolution pores, etc.), and micropores. Furthermore, the pore size distribution curve shows that the radii of macropores, mesopores, and micropores in type I are distributed in different ranges. The distribution features of type I's pore radius are the same as the features of D , and this indicates that our classification is reasonable. Both type II and type III have one fractal feature (Figures 12(b) and 12(c)). The fractal dimension of pore type II is between 2.85 and 2.50, with an average of 2.71, and as the value is close to 3, it indicates that the pore structure is more complex. However, the D of type III is 2.43–2.33, with an average of 2.39, indicating that the pore structure is relatively simple. Type III mainly consists of planktonic foraminifera intrafossil pores, so it leads to a homogeneous pore network and lower value of D . The D in type IV is mainly between 2.35 and 1.95, with an average of 2.1, very close to 2 (Figure 12(d)). This means, as per Cai et al.'s research, that the D of these pore types mainly reflects the characteristics of the micropore surface [70, 72]. In general, the D of the 4 pore structure types have obvious differences, and the values of D are consistent with the characteristics of the pore structures, indicating the rationality of the pore structure classification.

The correlation analysis of D with different pore throat structure parameters shows that the SC has the highest correlation with D (Figure 13). Although permeability, throat radius, FZI, and RQI are all related to D , the correlation coefficient is relatively low. The positive correlation between K and D indicates that a more homogeneous pore network is beneficial to the permeability of the reservoir. The correlation between porosity and D is the lowest, and it indicates that the complexity of pore structure has little correlation with the

volume of pores, and even a reservoir's pore network with low porosity can be very complex.

5.2. Permeability Prediction Models and Validation. Rock permeability is determined by many factors, not only porosity. Cai et al. pointed out that porosity, throat curvature, and throat size are all important factors affecting permeability [73]. The different throat structures in the pores have different pore permeability relationships. The porosity and permeability relationship constructed from the pore structure type is illustrated in Table 5. Each group has its own permeability-porosity relationship, and this could be used to calculate the permeability of noncoring wells. The results from the permeability predictions on two wells are shown in Figure 14. These results were obtained on the assumption that these wells had been logged and did not have core data, while in reality, the core data was available from the unpublished data at these wells. This was only done this way in order to check how accurately the method would predict the permeability in these wells had they not been cored. As seen, the profiles of the log-derived pore structure and permeability calculations agree with the core data.

5.3. Control Factors of Pore Structure. In general, diagenesis will continue to transform the original pore throat structure that was formed during the sedimentary period [74, 75]. Because of the active nature of the minerals in carbonate rocks, the pores in the reservoir rocks can be completely changed [5]. The sedimentary microfacies in the study area have been identified in previous studies, and the sedimentary environment was taken as the controlling factor of reservoirs [44, 45]. This study found that the pore structures that formed in different sedimentary environments were obviously different from each other (Figures 4 and 15, Table 3). Type I was formed in high-energy pellet shoal, and type II in a low-energy bioclastic shoal and intershoal sea. There is an erosion surface at the bottom of Kh₂₋₂ (Figure 15) as the nonselective dissolution of fresh water expands the throat and increases the permeability. The above indicates that the reservoir has been altered by dissolution. This transformation only exists in some local high lands however, such as in bioclastic shoal; therefore, the transformation of the pore's throat structure by means of diagenesis is determined by sedimentation. Type III was formed in open sea with foraminifera intrafossil pores for the main part, and the size of these pores was determined by the size of the foraminifera. The reason shall be attributed to the environment of foraminifera growth. Therefore, in general, the controlling factor for the reservoirs in the study area is sedimentation, while diagenesis, such as dissolution, also greatly changes the pore structure, which affects the porosity-permeability relationship.

6. Conclusion

There are many types of pore in the study area, and the combination of these pore types leads to a complex pore structure. In order to further understand the study area's complex pore throat structure and obtain a better permeability prediction model, this paper integrates the results from

the analysis on the rock thin section, SEM, HPMI, and NMR and uses a variety of parameters to study the pore structure. Then, the effectiveness of the pore structure classification is proven by D . This paper also puts forward a better permeability prediction model. The specific conclusions are as follows.

The reservoir is dominated by intergrain pores, moldic pores, intrafossil pores, intragrain dissolution pores, and micropores. There are six rock types, among which grainstone, algal packstone, algal wackestone, and foraminifera wackestone are porous rock types, and echinoderm wackestone and mudstone are nonporous rock types.

The pore structure types in the study area can be divided into four types: the mid-high-porosity, medium-high-permeability, and large-throat type (type I); the mid-high-porosity, midpermeability, and fine-throat type (type II); the mid-high-porosity, low-permeability, and fine-throat type (type III); and the low-porosity, low-permeability, and fine-throat type (type IV). In these 4 types, it is clear that the seepage capacity becomes worse with each one in turn. Among these types, the first three have the ability to store hydrocarbon, with their main reservoir spaces being intergrain pores, moldic pores, and intrafossil pores, respectively.

It is inaccurate to divide the reservoir's pore structure type by permeability and porosity alone. The comprehensive characterization of porosity, permeability, r_{apex} , S_{wm} , FZI, and RQI can be used to quantitatively divide the four pore structure types that are present in the study area very well, and the effectiveness of this pore structure classification proves the pore structure classification.

Each pore structure shows a good correlation between porosity and permeability. Additionally, we also proposed a permeability prediction model that showed good prediction effects.

The pore structure found in the reservoir rocks in the study area is mainly controlled by sedimentation, while diagenesis, such as dissolution, also greatly changes the pore structure, which in turn affects the porosity-permeability relationship.

Data Availability

All data used in the paper can be obtained from the author with consent.

Conflicts of Interest

The authors declare that there is no conflict of interest regarding the publication of this paper.

Authors' Contributions

Hao Lu and Hongming Tang engaged in pore structure research.

Acknowledgments

This research was funded by the Science and Technology Cooperation Project of the CNPC-SWPU Innovation Alli-

ance and general projects of the National Natural Science Foundation of China (No. 51674211).

References

- [1] P. O. Roehl and P. W. Choquette, *Carbonate Petroleum Reservoirs*, Springer-Verlag, 1985.
- [2] J. Garland, J. Neilson, S. E. Laubach, and K. J. Whidden, "Advances in carbonate exploration and reservoir analysis," *Geological Society, London, Special Publications*, vol. 370, no. 1, pp. 1–15, 2012.
- [3] C. Garing, L. Luquot, P. A. Pezard, and P. Gouze, "Electrical and flow properties of highly heterogeneous carbonate rocks," *AAPG Bulletin*, vol. 98, no. 1, pp. 49–66, 2014.
- [4] J. H. Norbistrath, R. J. Weger, and G. P. Eberli, "Complex resistivity spectra and pore geometry for predictions of reservoir properties in carbonate rocks," *Journal of Petroleum Science & Engineering*, vol. 151, pp. 455–467, 2017.
- [5] C. M. Burberry and M. H. Peppers, "Fracture characterization in tight carbonates: an example from the Ozark Plateau, Arkansas," *AAPG Bulletin*, vol. 101, no. 10, pp. 1675–1696, 2017.
- [6] M. Wang, H. Tang, F. Zhao et al., "Controlling factor analysis and prediction of the quality of tight sandstone reservoirs: a case study of the He8 member in the eastern Sulige gas field, Ordos Basin, China," *Journal of Natural Gas Science and Engineering*, vol. 46, pp. 680–698, 2017.
- [7] M. Wang, H. Tang, H. Tang et al., "Impact of differential densification on the pore structure of tight gas sandstone: evidence from the Permian Shihezi and Shanxi formations, eastern Sulige gas field, Ordos Basin, China," *Geofluids*, vol. 2019, no. 2, 25 pages, 2019.
- [8] G. R. Chalmers, "Characterization of gas shale pore systems by porosimetry, pycnometry, surface area, and field emission scanning electron microscopy/transmission electron microscopy image analyses: examples from the Barnett, Woodford, Haynesville, Marcellus, and Doig units," *AAPG Bulletin*, vol. 96, no. 6, pp. 1099–1119, 2012.
- [9] S. Mayo, M. Josh, Y. Nesterets et al., "Quantitative microporosity characterization using synchrotron micro-Ct and xenon K-edge subtraction in sandstones, carbonates, shales and coal," *Fuel*, vol. 154, pp. 167–173, 2015.
- [10] H. P. Menke, B. Bijeljic, M. G. Andrew, and M. J. Blunt, "Dynamic three-dimensional pore-scale imaging of reaction in a carbonate at reservoir conditions," *Environmental Science & Technology*, vol. 49, no. 7, pp. 4407–4414, 2015.
- [11] Y. Zhang, S. Jin, Y. Wang, and Y. Wang, "Characterization of the pore size distribution with SEM images processing for the tight rock," in *Paper presented at the 2015 IEEE International Conference on Information and Automation (ICIA)*, Lijiang, China, 2015.
- [12] P. Mostaghimi, M. Liu, and C. H. Arns, "Numerical simulation of reactive transport on micro-Ct images," *Mathematical Geosciences*, vol. 48, no. 8, pp. 963–983, 2016.
- [13] P. Wang, Z. Jiang, W. Ji et al., "Heterogeneity of intergranular, intraparticle and organic pores in Longmaxi shale in Sichuan Basin, South China: evidence from SEM digital images and fractal and multifractal geometries," *Marine and Petroleum Geology*, vol. 72, pp. 122–138, 2016.
- [14] J. O. Amaefule, M. Altunbay, D. Tiab, D. G. Kersey, and D. K. Keelan, "Enhanced reservoir description: using core and log

- data to identify hydraulic (flow) units and predict permeability in uncored intervals/wells," in *SPE annual technical conference and exhibition*, Houston, Texas, USA, 1993.
- [15] F. J. Lucia, *Carbonate Reservoir Characterization*, Springer, 2007.
- [16] L. M. Anovitz and D. R. Cole, "Characterization and analysis of porosity and pore structures," *Reviews in Mineralogy and Geochemistry*, vol. 80, no. 1, pp. 61–164, 2015.
- [17] B. S. Nabawy, Y. Géraud, P. Rochette, and N. Bur, "Pore-throat characterization in highly porous and permeable sandstones," *AAPG Bulletin*, vol. 93, no. 6, pp. 719–739, 2009.
- [18] M. Tucker, "Carbonate reservoirs: porosity evolution and diagenesis in sequence stratigraphic framework," *Organic Geochemistry*, vol. 32, no. 11, p. 1373, 2001.
- [19] M. Skalinski and J. A. M. Kenter, "Carbonate petrophysical rock typing: integrating geological attributes and petrophysical properties while linking with dynamic behaviour," *Geological Society, London, Special Publications*, vol. 406, no. 1, pp. 229–259, 2015.
- [20] H. A. Nooruddin and M. E. Hossain, "Modified Kozeny–Carmen correlation for enhanced hydraulic flow unit characterization," *Journal of Petroleum Science and Engineering*, vol. 80, no. 1, pp. 107–115, 2011.
- [21] E. L. Etris, D. S. Brumfield, R. Ehrlich, and S. J. Crabtree, "Relations between pores, throats and permeability: a petrographic/physical analysis of some carbonate grainstones and packstones," *Carbonates and Evaporites*, vol. 3, no. 1, pp. 17–32, 1988.
- [22] J. J. Funk, M. C. Choinski, B. B. Saxman, and C. A. Callender, "Characterization of carbonate porosity using petrophysical properties and image analysis," in *Middle East Oil Show*, Society of Petroleum Engineers, 1989.
- [23] C. M. Ross, C. A. Callender, J. B. Turbeville, and J. J. Funk, "Modeling of capillary pressure behavior using standard open hole wireline log data: demonstrated on carbonates from the Middle East," in *SPE Annual Technical Conference and Exhibition*, Dallas, Texas, USA, 1995.
- [24] I. Marzouk, H. Takezaki, and M. Suzuki, "New classification of carbonate rocks for reservoir characterization," in *Abu Dhabi International Petroleum Exhibition and Conference*, New Orleans, Louisiana, USA, 1998.
- [25] D. L. Cantrell and R. M. P. Hagerty, "Microporosity in Arab formation carbonates, Saudi Arabia," *GeoArabia*, vol. 4, no. 2, pp. 129–154, 1999.
- [26] E. A. Clerke, H. W. Mueller, E. C. Phillips et al., "Application of Thomeer hyperbolas to decode the pore systems, facies and reservoir properties of the upper Jurassic Arab D limestone, Ghawar Field, Saudi Arabia: a "Rosetta stone" approach," *GeoArabia*, vol. 13, no. 4, pp. 113–160, 2008.
- [27] X. Li, H. Huang, and L. Hao, "Improving the accuracy of permeability prediction modeling based on flow units: an example from the Khasib Limestone Reservoir of Ahdeb Oil Field, Iraq," *Paper presented at the SEG Technical Program Expanded Abstracts 2018*, 2018.
- [28] E. D. Pittman, "Relationship of porosity and permeability to various parameters derived from mercury injection-capillary pressure curves for sandstone (1)," *AAPG Bulletin*, vol. 76, 1992.
- [29] J. Lai, G. Wang, J. Cao et al., "Investigation of pore structure and petrophysical property in tight sandstones," *Marine and Petroleum Geology*, vol. 91, pp. 179–189, 2018.
- [30] K. Zhang, X. Pang, Z. Zhao et al., "Pore structure and fractal analysis of lower carboniferous carbonate reservoirs in the Marsel Area, Chu-Sarysu Basin," *Marine and Petroleum Geology*, vol. 93, pp. 451–467, 2018.
- [31] J. Lai, G. Wang, Z. Fan et al., "Insight into the pore structure of tight sandstones using NMR and HPMI measurements," *Energy & Fuels*, vol. 30, no. 12, pp. 10200–10214, 2016.
- [32] G. R. Coates and D. Miller, "Using NMR logs to reconstruct Sp and confirm R," *The Log Analyst*, vol. 39, no. 3, 1998.
- [33] G. Carneiro, A. Souza, A. Boyd, L. Schwartz, and V. Machado, "Evaluating pore space connectivity by NMR diffusive coupling," *SPWLA 55th Annual Logging Symposium, Society of Petrophysicists and Well-Log Analysts. Abu Dhabi*, 2014.
- [34] Y. Wang, H. Tang, M. Zheng, G. Tian, and Southwest Petroleum University, "The limitation of NMR to characterize the pore structure and irreducible water saturation of carbonate rocks: an experimental analysis," *Marine Origin Petroleum Geology*, vol. 23, no. 3, pp. 89–96, 2018.
- [35] D. Benavente, C. Pla, N. Cueto et al., "Predicting water permeability in sedimentary rocks from capillary imbibition and pore structure," *Engineering Geology*, vol. 195, pp. 301–311, 2015.
- [36] N. Zhang, M. He, B. Zhang, F. Qiao, H. Sheng, and H. Qinhong, "Pore structure characteristics and permeability of deep sedimentary rocks determined by mercury intrusion porosimetry," *Journal of Earth Science*, vol. 27, no. 4, pp. 670–676, 2016.
- [37] T. K. Al-Ameri, "Khasib and Tannuma oil sources, East Baghdad Oil Field, Iraq," *Marine and Petroleum Geology*, vol. 28, no. 4, pp. 880–894, 2011.
- [38] B. A. Al-Baldawi, "Petrophysical evaluation study of Khasib Formation in Amara Oil Field, South Eastern Iraq," *Arabian Journal of Geosciences*, vol. 8, no. 4, pp. 2051–2059, 2015.
- [39] G. Konert, "The petroleum geology of Iraq," *Journal of Petroleum Geology*, vol. 33, no. 4, p. 405, 2010.
- [40] A. A. M. Aqrabi, T. A. Mahdi, G. H. Sherwani, and A. D. Horbury, "Characterisation of the mid-Cretaceous Mishrif reservoir of the southern Mesopotamian Basin, Iraq," in *Paper presented at the American Association of Petroleum Geologists Conference and Exhibition*, Calgary, Alberta, Canada, 2010.
- [41] C. Hollis, "Diagenetic controls on reservoir properties of carbonate successions within the Albian–Turonian of the Arabian plate," *Petroleum Geoscience*, vol. 17, no. 3, pp. 223–241, 2011.
- [42] W. Zhou, R. Guo, M. Y. Fu, W. L. Chen, and R. C. Xie, "Characteristics and origin of Cretaceous limestone reservoir with bio-moldic pore and intrafossil pore, in Ahdeb Oilfield, Iraq," *Acta Petrologica Sinica*, vol. 30, no. 3, pp. 813–821, 2014.
- [43] B. J. Al Qayim, "Sequence stratigraphy and reservoir characteristics of the Turonian-Coniacian Khasib Formation in Central Iraq," *Journal of Petroleum Geology*, vol. 33, no. 4, pp. 387–403, 2010.
- [44] B. J. Al-Qayim, "Reservoir facies and sequence stratigraphy of the Khasib Formation in selected fields from Central Iraq," *GEO 2010: European Association of Geoscientists & Engineers*, 2010.
- [45] B. Al Qayim and F. Rashid, "Reservoir characteristics of the Albian Upper Qamchuqa Formation carbonates, Taq Taq oil-field, Kurdistan, Iraq," *Journal of Petroleum Geology*, vol. 35, no. 4, pp. 317–341, 2012.
- [46] A. A. Abed, "Hydraulic flow units and permeability prediction in a carbonate reservoir, Southern Iraq from well log data using non-parametric correlation," *International Journal of*

- Enhanced Research in Science Technology & Engineering*, vol. 3, no. 1, pp. 480–486, 2014.
- [47] H. Rahimpour-Bonab, B. Esrafil-Dizaji, and V. Tavakoli, “Dolomitization and anhydrite precipitation in Permian-Triassic carbonates at the South Pars Gasfield, offshore Iran: controls on reservoir quality,” *Journal of Petroleum Geology*, vol. 33, no. 1, pp. 43–66, 2010.
- [48] T. A. Mahdi, A. A. M. Aqrabi, A. D. Horbury, and G. H. Sherwani, “Sedimentological Characterization of the mid-Cretaceous Mishrif reservoir in Southern Mesopotamian Basin, Iraq,” *Geoarabia*, vol. 18, no. 1, pp. 139–174, 2013.
- [49] T. A. Mahdi and A. A. M. Aqrabi, “Sequence stratigraphic analysis of the mid-Cretaceous Mishrif Formation, southern Mesopotamian Basin, Iraq,” *Journal of Petroleum Geology*, vol. 37, no. 3, pp. 287–312, 2014.
- [50] J. Wang, D. Yang, X. Shu et al., “Flow unit identification and distribution in upper cretaceous of the Khasib Formation in a oilfield, Central Iraq,” *Geological Science & Technology Information*, vol. 35, no. 5, pp. 154–162, 2016.
- [51] F. Rashid, P. W. J. Glover, P. Lorinczi, R. Collier, and J. Lawrence, “Porosity and permeability of tight carbonate reservoir rocks in the north of Iraq,” *Journal of Petroleum Science and Engineering*, vol. 133, pp. 147–161, 2015.
- [52] C. Zhang, Z. Chen, and Z. Zhang, “Fractal characteristics of reservoir rock pore structure based on NMR T2 distribution,” *Journal of Oil and Gas Technology*, vol. 2007, no. 4, pp. 80–86, 2007.
- [53] X. Liang and W. Zhang, “A new method to construct reservoir capillary pressure curves using NMR log data and its application,” *Applied Geophysics*, vol. 5, no. 2, pp. 92–98, 2008.
- [54] X. Ge, Y. Fan, J. Li, and M. A. Zahid, “Pore structure characterization and classification using multifractal theory— an application in Santanghu Basin of western China,” *Journal of Petroleum Science and Engineering*, vol. 127, pp. 297–304, 2015.
- [55] A. Dillinger and L. Esteban, “Experimental evaluation of reservoir quality in Mesozoic formations of the Perth Basin (Western Australia) by using a laboratory low field nuclear magnetic resonance,” *Marine and Petroleum Geology*, vol. 57, pp. 455–469, 2014.
- [56] E. Müller-Huber, N. Jürgen Sch, and F. B. Rner, “Pore space characterization in carbonate rocks – approach to combine nuclear magnetic resonance and elastic wave velocity measurements,” *Journal of Applied Geophysics*, vol. 127, pp. 68–81, 2016.
- [57] R. J. Dunham, “Classification of carbonate rocks according to depositional texture,” *Mem. amer. assoc. petrol. geol.*, vol. 1, pp. 108–121, 1962.
- [58] F. J. Lucia, “Rock-fabric/petrophysical classification of carbonate pore space for reservoir characterization,” *AAPG Bulletin*, vol. 79, no. 9, pp. 1275–1300, 1995.
- [59] R. Rezaee, A. Saeedi, and B. Clennell, “Tight gas sands permeability estimation from mercury injection capillary pressure and nuclear magnetic resonance data,” *Journal of Petroleum Science and Engineering*, vol. 88–89, pp. 92–99, 2012.
- [60] M. Schmitt, C. P. Fernandes, F. G. Wolf, D. C. N. J. Bellini, C. P. Rahner, and S. D. S. V. Sampaio, “Characterization of Brazilian tight gas sandstones relating permeability and Angstrom-to micron-scale pore structures,” *Journal of Natural Gas Science & Engineering*, vol. 27, no. part_P2, pp. 785–807, 2015.
- [61] X. Tian, L. Cheng, R. Cao et al., “A new approach to calculate permeability stress sensitivity in tight sandstone oil reservoirs considering micro-pore-throat structure,” *Journal of Petroleum Science & Engineering*, vol. 133, pp. 576–588, 2015.
- [62] W. Huang, S. Lu, and S. H. Osman, “Quality grading system for tight sandstone reservoirs in the Quantou 4 Member, Southern Songliao Basin, Northeast China,” *Interpretation*, vol. 5, no. 4, pp. T503–T522, 2017.
- [63] G. Alves, E. Corrêa, P. N. Da Silva et al., “Prediction of carbonate rock type from NMR responses using data mining techniques,” *Journal of Applied Geophysics*, vol. 140, pp. 93–101, 2017.
- [64] G. Lesniak and P. Such, “Fractal approach, analysis of images and diagenesis in pore space evaluation,” *Natural resources research*, vol. 14, no. 4, pp. 317–324, 2005.
- [65] K. E. Higgs, M. J. Arnot, and S. Brindle, “Advances in grain-size, mineral, and pore-scale characterization of lithic and clay-rich reservoirs,” *AAPG Bulletin*, vol. 99, no. 7, pp. 1315–1348, 2015.
- [66] M. Freire-Gormaly, J. S. Ellis, H. L. MacLean, and A. Bazylak, “Pore structure characterization of Indiana limestone and pink dolomite from pore network reconstructions,” *Oil & Gas Science and Technology*, vol. 71, no. 3, p. 33, 2016.
- [67] Y. Rafiei and M. Motie, “Permeability evaluation on oil-window shale based on hydraulic flow unit: a new approach,” *Advances in Geo-Energy Research*, vol. 3, no. 3, pp. 277–286, 2019.
- [68] P. Zhang, S. Lu, J. Li, J. Zhang, H. Xue, and C. Chen, “Improved reservoir characterization by employing hydraulic flow unit classification in one of Iranian carbonate reservoirs,” *Advances in Geo-Energy Research*, vol. 3, no. 3, pp. 1067–1081, 2018.
- [69] P. Zhao, Z. Wang, Z. Sun, J. Cai, and W. Liang, “Investigation on the pore structure and multifractal characteristics of tight oil reservoirs using NMR measurements: Permian Lucaogou Formation in Jimusaer Sag, Junggar Basin,” *Marine and Petroleum Geology*, vol. 86, pp. 1067–1081, 2017.
- [70] F. Wang, K. Yang, and J. Cai, “Fractal characterization of tight oil reservoir pore structure using nuclear magnetic resonance and mercury intrusion porosimetry,” *Fractals-Complex Geometry Patterns and Scaling in Nnature and Society*, vol. 26, no. 2, p. 1840017, 2018.
- [71] K. Li, “Analytical derivation of Brooks-Corey type capillary pressure models using fractal geometry and evaluation of rock heterogeneity,” *Journal of Petroleum Science and Engineering*, vol. 73, no. 1–2, pp. 20–26, 2010.
- [72] J. Cai, W. Wei, X. Hu, R. Liu, and J. Wang, “Fractal characterization of dynamic fracture network extension in porous media,” *Fractals-Complex Geometry Patterns and Scaling in Nnature and Society*, vol. 25, no. 2, p. 1750023, 2017.
- [73] J. Cai, Z. Zhang, W. Wei, D. Guo, S. Li, and P. Zhao, “The critical factors for permeability-formation factor relation in reservoir rocks: pore-throat ratio, tortuosity and connectivity,” *Energy*, vol. 188, article 116051, 2019.
- [74] X. Lu, Y. Wang, D. Yang, and X. Wang, “Characterization of paleo-karst reservoir and faulted karst reservoir in Tahe oil-field, Tarim Basin, China,” *Advances in Geo-Energy Research*, vol. 4, no. 3, pp. 339–348, 2020.
- [75] H. Lu, H. Tang, M. Wang, and Y. Wang, “Characterization of a carbonate reservoir formed in a low energy environment,” *Journal of Coastal Research*, vol. 104, no. sp1, 2020.